Atmospheric
Chemistry
and Physics

NO$_x$ lifetimes and emissions of cities and power plants in polluted background estimated by satellite observations

Fei Liu[1,2,3], **Steffen Beirle**[3], **Qiang Zhang**[2], **Steffen Dörner**[3], **Kebin He**[1,2], **and Thomas Wagner**[3]

[1]State Key Joint Laboratory of Environment Simulation and Pollution Control, School of Environment, Tsinghua University, Beijing 100084, China
[2]Ministry of Education Key Laboratory for Earth System Modeling, Center for Earth System Science, Tsinghua University, Beijing 100084, China
[3]Max-Planck-Institut für Chemie, Mainz 55128, Germany

Correspondence to: S. Beirle (steffen.beirle@mpic.de) and Q. Zhang (qiangzhang@tsinghua.edu.cn)

Abstract. We present a new method to quantify NO$_x$ emissions and corresponding atmospheric lifetimes from OMI NO$_2$ observations together with ECMWF wind fields without further model input for sources located in a polluted background. NO$_2$ patterns under calm wind conditions are used as proxy for the spatial patterns of NO$_x$ emissions, and the effective atmospheric NO$_x$ lifetime is determined from the change of spatial patterns measured at larger wind speeds. Emissions are subsequently derived from the NO$_2$ mass above the background, integrated around the source of interest.

Lifetimes and emissions are estimated for 17 power plants and 53 cities located in non-mountainous regions across China and the USA. The derived lifetimes for the ozone season (May–September) are 3.8 ± 1.0 h (mean $\pm$ standard deviation) with a range of 1.8 to 7.5 h. The derived NO$_x$ emissions show generally good agreement with bottom-up inventories for power plants and cities. Regional inventory shows better agreement with top-down estimates for Chinese cities compared to global inventory, most likely due to different downscaling approaches adopted in the two inventories.

1 Introduction

Nitrogen oxides (NO$_x$) are toxic air pollutants and play an important role in tropospheric chemistry as precursors of tropospheric ozone and secondary aerosols (Jacob et al., 1996; Seinfeld and Pandis, 2006). Power plants and cities with large vehicle populations and intense industrial activities are significant anthropogenic emitting sources of NO$_x$. Accurate knowledge of NO$_x$ emissions on urban scales is thus a critical factor for accurate bottom-up emission inventories, which are important inputs for chemical transport models (CTMs) and for the development of mitigation strategies.

Bottom-up emission inventories depend on information of fuel consumptions and emission factors, which are subject to substantial uncertainties (Butler et al., 2008; Zhao et al., 2011). A significant improvement in accuracy of emission inventories for power plants has been achieved by the installation of continuous emissions monitoring systems (CEMSs). For example, in the USA, under the 1990 Clean Air Act, power plant operators are required to install an automated data acquisition and handling system for measuring and recording pollutant concentrations from plant exhaust stacks and follow the monitoring regulations to ensure that the reported emission data are consistent and of high quality (Kim et al., 2009). For countries where reliable CEMS data are not available (like China), activity rates and emission factors can be adopted at plant level to improve the accuracy of power plant emissions (e.g., Zhao et al., 2008; Liu et al., 2015). However, developing emission inventories for individual cities with high accuracy faces enormous challenges, considering the lack of a complete and reliable database including fuel consumptions and emission factors at city level. Emissions at city level are often downscaled from regional emission estimates, based on surrogates (e.g., population density, industrial productivity) that, however, often just

roughly reflect the magnitude and spatial distribution of urban emissions. Thus, independent emission estimates would be a desirable complement to validate and improve existing emission inventories.[1]

The NO$_2$ tropospheric vertical column densities (TVCDs; the vertically integrated concentration in the troposphere) retrieved from satellite measurements provide valuable global information on the spatiotemporal patterns of NO$_x$, including trends (e.g., Richter et al., 2005; Schneider and van der A, 2012; Hilboll et al., 2013), responses of NO$_2$ level changes to air quality control, economic and political factors (e.g., Duncan et al., 2013; Lelieveld et al., 2015), and temporal variations like weekly cycles in NO$_2$ TVCDs (Beirle et al, 2003; Russell et al., 2010; Valin et al., 2014). In addition, the satellite NO$_2$ measurements have been applied to quantify NO$_x$ emissions. In a pioneering study (Leue et al., 2001), the downwind decay of NO$_2$ TVCDs in continental outflow regions was used to estimate a (constant) NO$_x$ lifetime, which was then applied to project global NO$_x$ emissions from the measured mean NO$_2$ TVCDs. Later on, CTMs were employed to exploit satellite observations as a constraint towards improving NO$_x$ emission inventories (e.g., Martin et al., 2003; Konovalov et al., 2006; Kim et al., 2009; Lamsal et al., 2011). The derived top-down inventories show pronounced differences relative to bottom-up estimates and their accuracy has been validated by the improved performance of model simulations with respect to in situ measurements (e.g., Martin et al., 2006). However, the top-down inventories are usually determined at regional/global scale related to the spatial resolution of CTMs, while the spatial scales relevant for individual emission hot spots (power plants or cities) are not resolved. In addition, modeled lifetimes have large uncertainties (Lin et al., 2012) due to the highly nonlinear small-scale chemistry in urban areas, and they are thus probably not appropriate for relating NO$_2$ TVCDs to NO$_x$ emission rates at city level.

With the launch of the Ozone Monitoring Instrument (OMI) (Levelt et al., 2006) with high spatial resolution (13 × 24 km^2 at nadir), individual large sources like megacities and power plants can be resolved. In a recent study, Beirle et al. (2011) averaged OMI NO$_2$ measurements separately for different wind directions, thereby constructing clear downwind plumes which allow a simultaneous fit of the effective NO$_x$ lifetimes and emissions, without the need of a chemical model. Valin et al. (2013) adopted this approach but rotated satellite NO$_2$ observations according to wind directions such that all the NO$_2$ columns are aligned in one direction (from upwind to downwind). The rotation procedure accumulated a statistically significant data set to examine the dependence of NO$_x$ lifetime on the wind speed. De Foy et

al. (2015) and Lu et al. (2015) adopted this plume rotation technique and quantified NO$_x$ emissions from isolated power plants and cities, respectively, over the USA which showed that the method can give reliable estimates over multi-annual averages and even provide estimates of emission trends with reasonable accuracy. De Foy et al. (2014) also analyzed the performance of the method using model simulations with fixed a priori lifetimes and realistic wind data, which proved that the model accurately estimated the synthetic emission, but did not necessarily accurately retrieve the lifetime, and showed best performance for strong wind cases. Alternative approaches based on model functions with multiple dimensions, e.g., a two-dimensional Gaussian function (Fioletov et al., 2011) and a three-dimensional function (Fioletov et al., 2015), were also proposed to estimate lifetimes and emissions.

However, so far all studies assume that the source of interest can be considered as a "point source", which works well for isolated sources like Riyadh, showing a high contrast against clean background with small and smooth TVCDs. However, for sources located in a heterogeneously polluted background, a modification of these methods is needed in order to account for the effect of interfering sources within small distances.

In this work, we present a new method for the quantification of NO$_x$ lifetimes and emissions for power plants and cities located in polluted background. The mean OMI NO$_2$ distribution for 2005–2013 is calculated separately for calm conditions as well as for different wind direction sectors according to ECMWF (European Center for Medium-range Weather Forecast) wind fields. The mean lifetime is derived from the change of the observed NO$_2$ patterns under windy versus calm conditions. NO$_x$ emissions of power plants and cities over China and the USA are subsequently quantified from the integrated TVCDs and the derived lifetimes and compared to bottom-up emission inventories.

2 Methodology

2.1 Satellite NO$_2$ data

We base this study on NO$_2$ TVCDs from the OMI tropospheric NO$_2$ (DOMINO) v2.0 product (Boersma et al., 2011), which is provided by the Tropospheric Emissions Monitoring Internet Service (TEMIS; see http://www.temis.nl/airpollution/no2.html). OMI is a UV–vis nadir-viewing satellite spectrometer (Levelt et al., 2006) on board the Aura satellite (Celarier et al., 2008), launched in 2004. NO$_2$ columns are derived from radiance measurements, using the Differential Optical Absorption Spectroscopy (DOAS) algorithm (Platt, 1994). OMI provides daily global coverage with a local equator crossing time of approximately 13:45. It detects radiance spectra from 60 across-track pixels with

---

[1] The emission data for US power plants, Chinese cities and US cities are accessible at https://www.epa.gov/energy/egrid, http://www.meicmodel.org and http://edgar.jrc.ec.europa.eu/overview.php?v=42, respectively.

ground pixel sizes ranging from $13 \times 24\,\text{km}^2$ at nadir to about $13 \times 150\,\text{km}^2$ at the outermost swath angle (57°).

The 10 outermost pixels on both sides of the swath are excluded in this study to limit the across-track pixel width $< 40\,\text{km}$. From June 2007, OMI has shown severe spurious stripes, known as row anomalies, that are likely caused by an obstruction in part of OMI's aperture (http://www.knmi. nl/omi/research/product/rowanomaly-background.php). The affected pixels are also excluded from the analysis. Only mostly cloud-free observations (effective cloud fraction $< 30\,\%$) are considered in this study.

Mean NO$_2$ TVCDs over the USA and China during "ozone season" (May–September) for 2005 to 2013 are calculated separately for calm (wind speed below $2\,\text{m\,s}^{-1}$) and eight different wind direction sectors following the approach in Beirle et al. (2011). We focus on the ozone season to include the photochemically relevant months for ozone production (USEPA, 2014) and to exclude the winter data with larger uncertainties due to larger solar zenith angles, variable surface albedo (snow), and longer NO$_x$ lifetime. Wind fields at a lat/long grid of 0.36° width are taken from the ECMWF ERA-Interim reanalysis (Dee et al., 2011, reanalysis data available at: http://www.ecmwf.int/en/ research/climate-reanalysis/era-interim), and the horizontal wind components of the lowermost 500 m are averaged. Individual clear-sky observations of NO$_2$ TVCDs are assigned to a $2 \times$ finer grid (0.18°, comparable to the extent of OMI ground pixels) according to the pixel center coordinates and are associated with the corresponding ECMWF wind fields interpolated in time.

2.2 NO$_2$ outflow models and lifetime/emission fits

In this section, we present a modified method compared to Beirle et al. (2011) for the determination of lifetimes and emissions for complex source distributions. The basic idea is to use the measured NO$_2$ spatial pattern under calm wind conditions as proxy for the distribution of NO$_x$ sources, instead of assuming a single point source.

Below, we (a) summarize the fitting procedure of Beirle et al. (2011) and demonstrate that this method cannot be applied for multiple sources (Sect. 2.2.1), (b) describe the model function for the modified lifetime fit (Sect. 2.2.2), and (c) eventually explain how emission rates are determined (Sect. 2.2.3).

We select Harbin (45.8° N, 126.7° E), the capital of Heilongjiang province in China, with a population of about 6 million (city) to 10 million (greater area) inhabitants, to demonstrate our approach. Harbin is a typical city located in a polluted background, surrounded by three other large NO$_x$ sources (i.e., the cities of Daqing, Jilin, and Changchun) within $\sim 200\,\text{km}$ radius. Figure 1 displays mean NO$_2$ TVCDs around Harbin for calm conditions (a), southerly wind (b), and their difference (c). The outflow plume of NO$_2$ from Harbin is not as clear as that from isolated sources (e.g., Riyadh in Beirle et al., 2011) due to the interferences from surrounding sources. However, the spatial pattern of their difference (Fig. 1c) still clearly reveals outflow patterns, consistent with ECMWF wind fields.

In order to investigate the downwind plume evolution, one-dimensional NO$_2$ "line densities", i.e., NO$_2$ per cm, are calculated as function of distance for each wind direction sector separately by integration of the mean NO$_2$ TVCDs (i.e., NO$_2$ per cm^2) perpendicular to the wind direction, as in Beirle et al. (2011).

2.2.1 Isolated point source outflow model: lifetime and emissions

In Beirle et al. (2011), a simple model function $M(x)$ (Eq. 1) was used to fit the observed line densities, which is composed of an exponential function $e(x)$ (Eq. 2) describing the transport pattern and chemical decay, and a Gaussian function $G(x)$ (Eq. 2) accounting for different effects causing spatial smoothing (e.g., the spatial extent of the source, the OMI ground pixel size, or wind fluctuations).

$$M(x) = E \times (e \otimes G)(x) + B \tag{1}$$

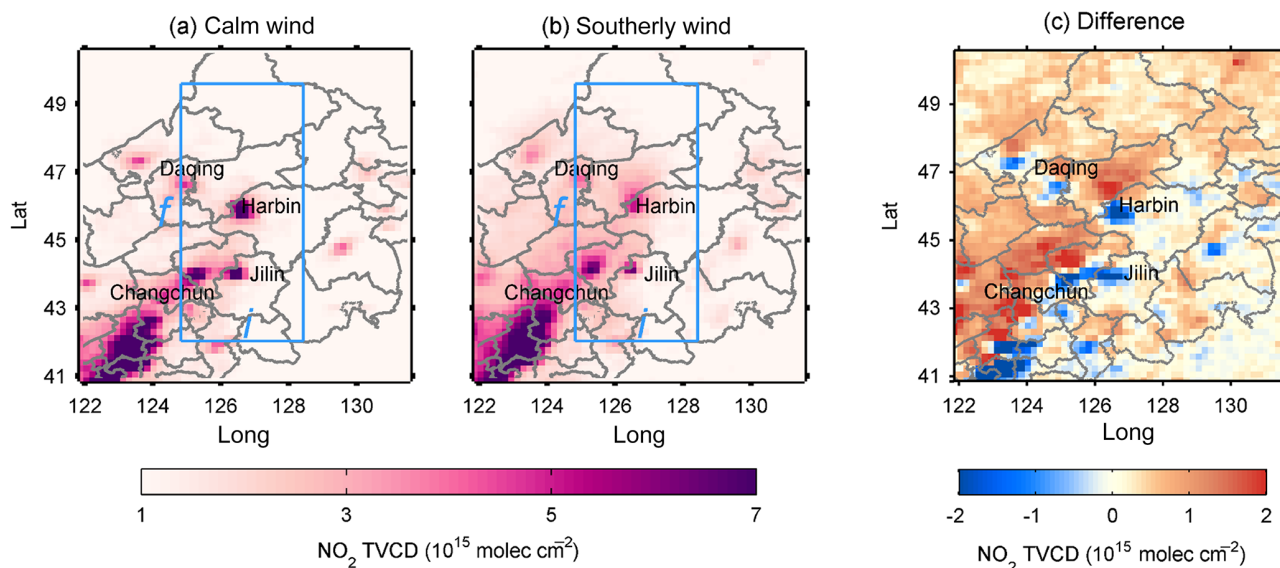$$e(x) = \exp\left(-\frac{x - X}{x_0}\right) \quad \text{for } x \geq X, \; 0 \text{ otherwise} \tag{2}$$

$$G(x) = \frac{1}{\sqrt{2\pi}\sigma} \exp\left(-\frac{x^2}{2\sigma^2}\right) \tag{3}$$

E represents total emissions, B represents a constant background, X is the location of the source (relative to the a priori coordinates of the site under investigation), x_0 is the e-folding distance downwind, and σ is the standard deviation of $G(x)$. The mean lifetime τ is derived from the e-folding distance x_0 by division by w, the mean projected wind speed. By this approach, emissions and lifetimes of NO$_2$ are fitted simultaneously.

Uncertainties are estimated from the confidence intervals of individual fits, the variability of fit results of the same location for different wind directions, and the dependency of a priori assumptions like fit intervals and the detailed choice for the applied wind data, as inferred from sensitivity studies (see the Supplement of Beirle et al., 2011, for details). In addition, the uncertainty of NO$_2$ TVCDs of about 30 % is transmitted to the final emission estimate. Final errors are of the order of 50 % for lifetimes and 60 % for emissions, with (i) the fit uncertainty, (ii) the uncertainties introduced by the applied wind data, and (iii) uncertainties for TVCDs (affecting only the emission estimate) being the most important contributions.

In Beirle et al. (2011) lifetime and emissions are derived for nine isolated hot spots exhibiting high NO$_2$ TVCDs over a clean background within about 200 km. However, this method cannot be applied to hot spots surrounded by additional significant sources, like Harbin (Fig. 1), as by definition the method can only represent a single "point source"

Figure 1. Mean NO$_2$ TVCDs around Harbin for **(a)** calm, **(b)** southerly wind conditions and **(c)** their difference (southerly – calm). For the fit of lifetimes, the mean NO$_2$ TVCDs are integrated over interval i in across-wind direction to calculate line densities and the fit is performed over the fit interval f (blue lines in **(a)** and **(b)**; see Sect. 2.2.2 for details).

convolved with a Gaussian function. For instance, an additional source at 100 km with only 10 % of the emissions of the source under investigation causes a lifetime bias of ∼ 20 %, as the fit tries to "explain" increased downwind values by a longer lifetime (see Fig. S1 and explanations in the Supplement). For an interfering source of the same order as the source of interest, the method fails completely.

2.2.2 Mixed source outflow model: lifetime

We develop an alternative method accounting for emissions from multiple sources. The patterns of line densities under windy conditions result from the transport, chemical decay, and spatial smoothing of emission patterns. The basic idea is to use the NO$_2$ patterns observed under calm conditions, $C(x)$, as proxy of emission patterns instead of assuming a single point source as in previous studies. Lifetime information is then obtained based on the observed change of the NO$_2$ patterns under windy versus calm conditions. Note that the one-dimensional pattern of line densities under calm conditions has to be determined along the same (wind) direction, for which the line densities under windy conditions are determined. That means that in total eight one-dimensional line densities under calm conditions are determined for the eight wind directions. However, only directions with reasonable reliability are considered where mean NO$_2$ line densities for both calm and windy conditions are well defined (i.e., gaps due to missing data are less than 10 % in the across-wind integration interval i and less than 20 % in the fit interval in wind direction f). We define the new model function $N(x)$

as

$$N(x) = a \times [e \otimes C](x) + b, \qquad (4)$$

where $e(x)$ is again a truncated exponential function (Eq. 2 with $X = 0$). The scaling factor a and offset b are included to account for possible systemic differences between windy and calm wind conditions (e.g., cloud conditions, vertical profiles, or lifetimes), which will be discussed in Sect. 3.1 in detail.

We perform a nonlinear least-squares fit of $N(x)$ to the observed line densities with a, b, and x_0 as fitting parameters. We set the fit interval in wind direction f to 600 km (300 km in downwind direction, which corresponds to 3 times of the e-folding distance for a lifetime of 5 h and a mean wind speed of 6 m s^{-1}). The across-wind integration interval i is set to be half (300 km). f and i are indicated in Fig. 1a and b. The intervals are larger than those in Beirle et al. (2011), since not only the source under investigation but also interfering sources have to be appropriately accounted for when comparing line densities of calm and windy conditions. We also perform fits with different intervals (±100 km, see Table S1) and find only small changes (∼ 10 %) for the resulting lifetimes.

Figure 2a displays the observed line densities for calm (blue) and southerly winds (red) around Harbin and the fitted model function $N(x)$ (grey). Generally, $N(x)$ describes the observed downwind patterns well: the coefficients of determination (R^2) between observation and fit are 0.96–0.99 with the range of 3.0–4.4 h for different wind directions, as shown in Fig. 2a–e.

Like in Beirle et al. (2011), the lifetime τ is derived by the ratio of the fitted e-folding distance and the mean wind speed[2]: $\tau = x_0/w$. For Harbin, τ is computed to be 3.9 h with a typical 95 % confidence interval (CI) of ± 0.6 h for southerly winds. Averaging the fit results for all wind direction sectors with a good fit performance (i.e., $R > 0.9$, lower bound of CI > 0, and CI width < 10 h,) yields $\tau = 3.5$ h with a standard deviation of 0.6 h (Fig. 2), using the fit residues as well as the CI of τ as inverse weights, as in Beirle et al. (2011).

Here we assumed that the removal of NO$_2$ can be simply described by a first order loss, and thus the chemical decay of NO$_2$ follows an exponential decay function $e(x)$ (Eq. 2) with an e-folding distance x_0, which yields an overall, effective lifetime τ. In Beirle et al. (2014), it was investigated how far the estimated lifetime by this approach might be biased in case of temporal fluctuations of both emissions and instantaneous lifetimes. The impact of such fluctuations was found to be rather small.

2.2.3 Mixed source outflow model: emissions

The modified fitting function $N(x)$ proved to be capable of gaining lifetime information even for complex source distributions. The interferences from multiple neighboring sources, which cannot be represented by a single-source Gaussian distribution, are successfully described by the new model function using $C(x)$ as proxy for the spatial distribution of NO$_x$ sources. However, in contrast to the previous fitting function $M(x)$ in Beirle et al. (2011), $N(x)$ does not contain the magnitude of NO$_x$ emissions directly, but only the emission pattern represented by NO$_2$ under calm conditions. Thus, total NO$_x$ emissions have to be estimated separately.

According to mass balance, the total mass of NO$_x$ equals the emission rate times lifetime. Emissions can thus be derived in a three-step approach by (a) integrating observed TVCDs originating from the source of interest to calculate the total mass of NO$_2$, (b) scaling NO$_2$ to NO$_x$, and (c) dividing by the lifetime τ, which was derived as described in the previous section.

a. Total NO$_2$ mass. In order to quantify the total NO$_2$ mass of the target source, the observed TVCDs have to be integrated around the source, in which (1) interferences with neighboring sources have to be avoided and (2) a polluted background has to be appropriately accounted for. Thus, we base the estimation of the total NO$_2$ mass

on the mean TVCDs under calm conditions, to minimize interferences by advection. Again, we calculate line densities by integrating the NO$_2$ TVCDs in "across-wind" direction[3], but for a smaller interval v representing the spatial extent of megacities or urban centers but excluding neighboring sources. Here we define $v = 40$ km. We then perform a nonlinear least-squares fit of a modified Gaussian function $g(x)$ to these line densities under calm wind condition, as illustrated in Fig. 3. The line densities integrated perpendicular to the different wind direction sectors are used to constrain the fitted A in $g(x)$:

$$g_i(x) = A \times \frac{1}{\sqrt{2\pi}\sigma_i} \exp\left(-\frac{(x-X)^2}{2\sigma_i^2}\right) + \varepsilon_i + \beta_i x, \quad (5)$$
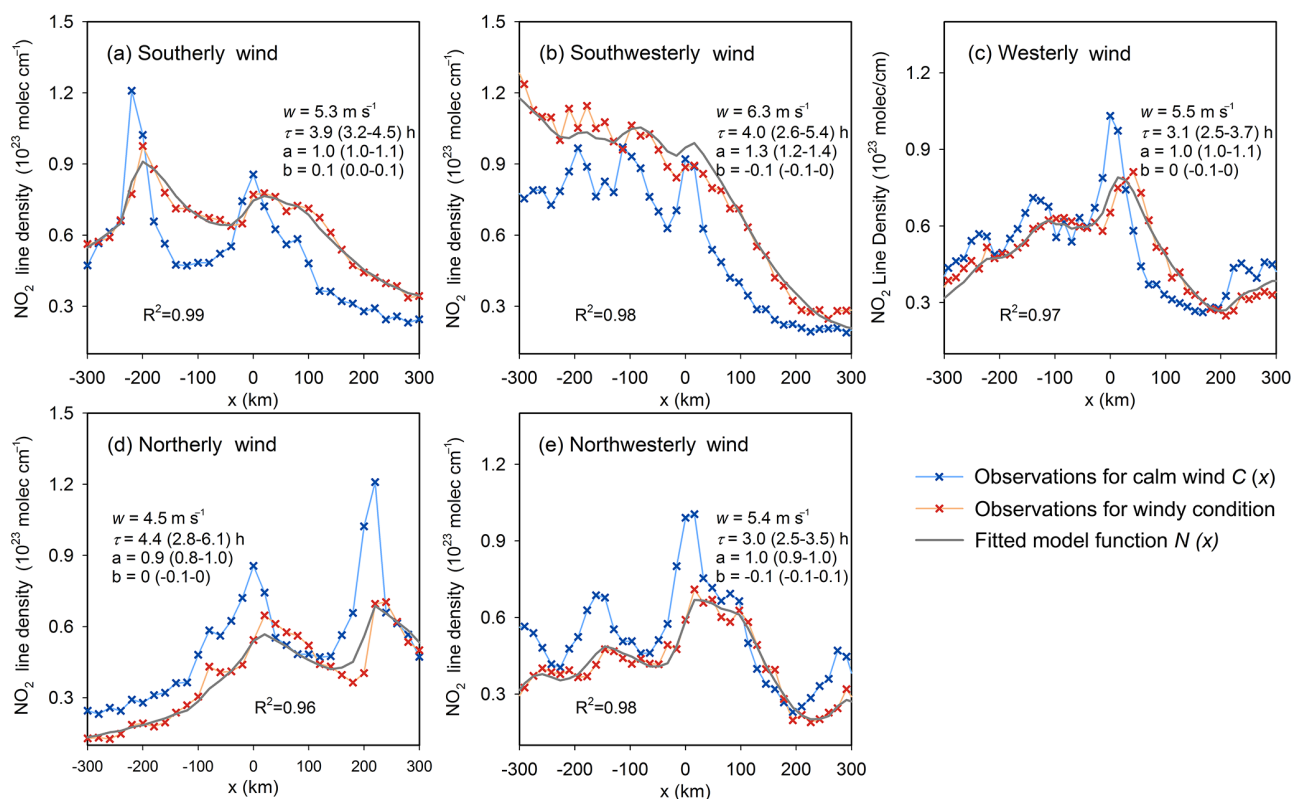
where i represents the wind direction sector. Note that the projections of line densities under calm wind conditions for opposite wind direction sectors, e.g., north and south, are just mirrored. Thus, we combined the projections for opposite wind direction sectors. That is, i represents southeast–northwest, south–north, southwest–northeast, and east–west. X is the location of the source (relative to the a priori coordinates of the site under investigation). σ_i is the standard deviation of the Gaussian $g_i(x)$, and ε_i and β_i represent an offset and a possible linear gradient in the background field, respectively. While the e-folding distance is fitted for each wind direction separately (and mean lifetimes might actually be different for each wind direction), the emissions are not expected to depend on wind direction. We thus use all available wind directions to perform one fit of all functions $g_i(x)$ simultaneously with wind-sector-dependent backgrounds, but one overall parameter A.

The NO$_2$ amount A (in molecules) around the source on top of the (wind-sector-dependent) background is determined by fitting the functions $g_i(x)$ simultaneously for all available wind directions.
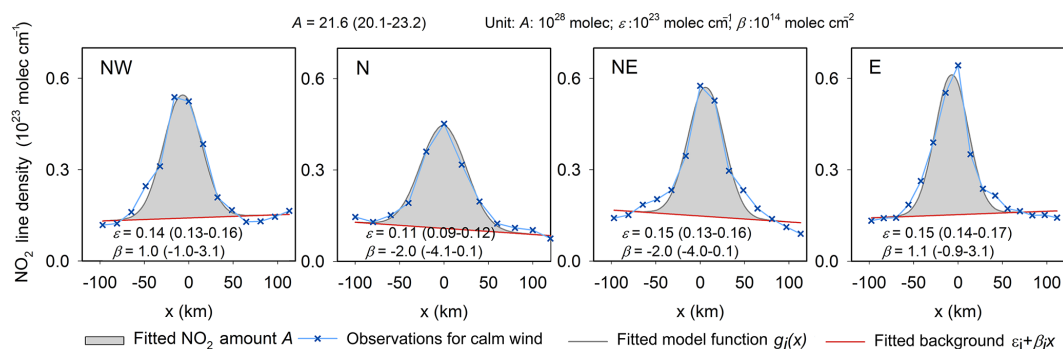
The fit of total NO$_2$ mass is performed over the interval h in wind direction (see Fig. S2). The fit interval h has to be chosen to be larger than v in order to allow for a meaningful fit of $g(x)$. We set h to 200 km for cities (see Fig. S2) and 100 km for power plants. The fit interval thus potentially includes interfering sources. However, these interferences are in first order accounted for by the linear variation of the background fitted in function $g_i(x)$. Note that the fit $g(x)$ is less sensitive to interfering sources compared to the original fit of $M(x)$ in Beirle et al. (2011), as lifetime is not involved here.

The small interval v (40 km) excludes neighboring sources but does not capture the full plume in across

---

[2]Note that we subtracted the residual mean wind speed under calm wind conditions from w in order to account for the subtle movement of $C(x)$ compared to the emission pattern; this is, however, a small effect (the relative change between τ determined by wind speeds with and without subtracting calm wind speeds is within -2–3 %). However, the effect could be larger for persistent winds and for larger thresholds for calm.

[3]Though focussing on calm conditions, we calculate the projections for different wind direction sectors analogue to the lifetime fit procedure.

Figure 2. NO$_2$ line densities around Harbin for different wind direction sectors. Crosses: NO$_2$ line densities for calm (blue) and **(a)** southerly, **(b)** southwesterly, **(c)** westerly, **(d)** northerly, and **(e)** northwesterly (red) winds as a function of the distance x to Harbin center. Grey line: the fit result $N(x)$. The numbers indicate the net mean wind velocities (windy – calm) from ECMWF (w), the lifetime τ, the factor a and offset b resulting from the least-squares fit with 95 % confidence interval. NO$_2$ line densities for the remaining wind direction sectors are dismissed due to missing data (see the criteria of "reliability" defined in Sect. 2.2.2).

Figure 3. NO$_2$ line densities in Harbin for northwest, north, northeast and east directions (from left to right). Crosses: NO$_2$ line densities for calm winds as a function of the distance to Harbin center x. Grey line: the fit result $g_i(x)$. Pink line: the fitted background $\varepsilon_i + \beta_i x$. Grey shade: the magnitude of the fitted NO$_2$ amount A. The number indicates A, the offset ε and the linear gradient in the background field β resulting from the least-squares fit with 95 % CI.

Table 1. Intervals chosen for the fit of the NO$_x$ lifetime and total mass.

Category	Interval (km)	
	Wind direction (fit)	Across-wind direction (integration)
Fit lifetime	f	i
	600	300
Fit total mass	h	v
Power plant	100	40
City	200	40
Pearl River Delta	300	60

wind direction due to dilution. This effect is corrected for by scaling A afterwards by a factor $f(\sigma_i)$ based on the fitted plume width σ_i:

$$f(\sigma_i) = \int\limits_{-20\,\text{km}}^{20\,\text{km}} \frac{1}{\sqrt{2\pi}\sigma_i} \exp\left(-\frac{(x-X)^2}{2\sigma_i^2}\right) \Big/ \quad (6)$$

$$\int\limits_{-\infty}^{\infty} \frac{1}{\sqrt{2\pi}\sigma_i} \exp\left(-\frac{(x-X)^2}{2\sigma_i^2}\right).$$

Note that we consider a larger interval (60 km for v and 300 km for h) for Pearl River Delta, which is a megalopolis covering nine prefectures over an area of about 56 000 km^2. We tabulated the intervals chosen for fits for different cases in Table 1.

The resulting emissions are rather insensitive with respect to modified settings for v and h (see Supplement, Sect. 3). Again, fit results with poor performance ($R < 0.9$, lower bound of CI < 0, CI width $> 0.8 \times A$) are discarded.

b. Scaling NO$_2$ to NO$_x$. According to the typical [NO] / [NO$_2$] ratio of 0.32 under urban conditions at noon (Seinfeld and Pandis, 2006), the total NO$_2$ mass is scaled by a factor of 1.32 in order to derive total NO$_x$ mass following Beirle et al. (2011).

c. Emission rates (NO$_x$ amount per time unit) are derived by dividing of the total NO$_x$ mass by the lifetime derived for the respective location as described in Sect. 2.2.2. For Harbin, the total mass (in terms of NO$_2$) is computed to be 33.2×10^{28} molec with a CI of 2.4×10^{28} molec. The total NO$_x$ emissions derived for Harbin are 58.1 mol s^{-1}.

2.3 Uncertainties

We define total uncertainties of the fitted lifetimes and emissions analogue to the procedure described in Beirle et

al. (2011), basically based on the fit performance and the dependencies on the a priori settings as investigated in sensitivity studies. Here we shortly list the main sources of uncertainties and how they are quantified. Further details are provided in Sect. 3 of the Supplement. The resulting quantitative error estimates are given and discussed below along with the derived lifetime and emission estimates.

The confidence intervals (CIs) resulting from the least-squares fits of Eq. (4) and Eq. (5) directly reflect the uncertainties of the derived lifetimes and emissions. In addition, the standard deviations of the fitted lifetimes for different wind direction sectors provide information on the consistency of the method. Both effects can be quantified straightforwardly and are included in the total uncertainty, contributing about 30 % for lifetimes and 20 % for emissions arising from CI and less than 40 % for both arising from standard mean error (see Sect. 3 of Supplement). The dependency on the a priori choices of integration and fit intervals is quantified based on sensitivity studies and found to be of the order of 10 %.
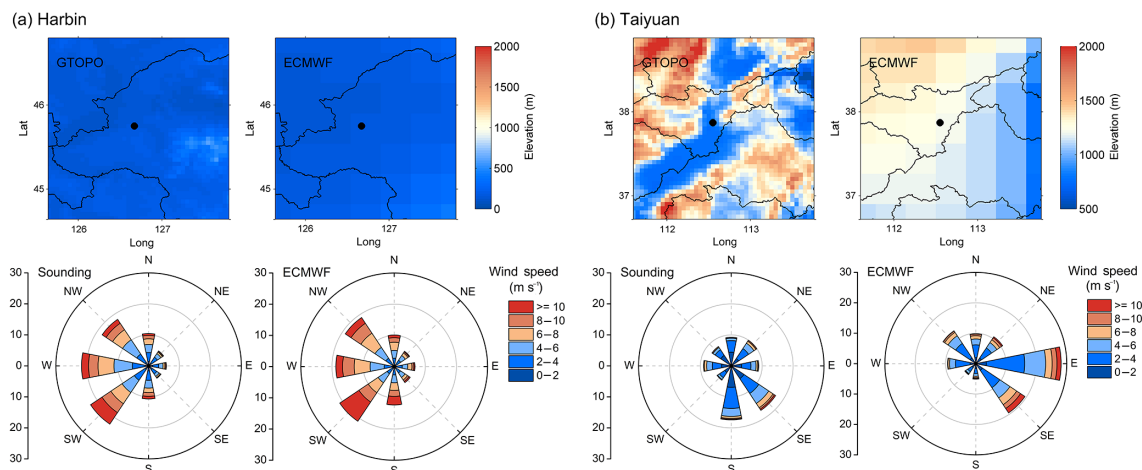
Accurate wind fields are required for the sorting procedure as well as for the conversion of the downwind decay from a function of distance into a function of time. Again, the impact of the a priori settings (horizontal ECMWF wind fields vertically integrated over the lowest 500 m) is estimated based on sensitivity studies. In addition, ECMWF wind fields have been checked by comparison to in situ sonde measurements, which generally agree well except over complex terrain (see Sect. 2.6). The comparison of projected wind speeds of from ECMWF and sonde measurements allows to estimate the uncertainty of the lifetime fit caused by uncertainties of both ECMWF wind speeds and direction. Overall, the uncertainty related to wind fields is about 30 %.

In addition, the derived emissions (but not the lifetime) are affected by the uncertainty of tropospheric NO$_2$ TVCDs (30 %; see Boersma et al., 2007 and Sect. 3e in the Supplement) and the NO$_2$ / NO$_x$ ratio (10 %). the uncertainty of tropospheric NO$_2$ TVCDs (30 %; see Boersma et al., 2007 and Sect. 3e in the Supplement).

In the Supplement, we also discuss sophisticated effects such as the potential dependence of lifetimes on wind conditions, the assumption of a constant NO$_2$ / NO$_x$ ratio, and the concept of a single lifetime describing the downwind evolution of NO$_2$ over several hours. These effects have been found to be rather small.

We define total uncertainties of the resulting lifetimes and emissions as the root of the quadratic sum of the above mentioned contributions, which are assumed to be independent.

Figure 4. Comparison of the topography (top panel) and wind roses (bottom panel) from ECMWF (right panel) and higher-resolution data sets (left panel) around **(a)** Harbin and **(b)** Taiyuan. The land surface elevation on the left panel is derived from GTOPO30. The wind roses on the left panel are generated from sounding measurements assembled by University of Wyoming. Radial units are percent per 45° direction band.

2.4 Bottom-up emission inventories

We use bottom-up emission inventories to pre-select promising sites and for a comparison to the derived top-down estimates. We select inventories that provide up-to-date, multi-year NO$_x$ emissions at high spatial resolution that are widely used in the community. The following inventories are considered: for power plants, we use the China coal-fired Power plant Emissions Database (CPED), developed by Liu et al. (2015) based on unit-level fuel consumptions and emission factors derived from various sources, and the US Emissions & Generation Resource Integrated Database (eGRID) using emissions derived from continuous emissions monitoring systems (available at https://www.epa.gov/energy/egrid) (USEPA, 2014). For cities, we use the Multi-resolution Emission Inventory for China (MEIC; http://www.meicmodel.org) compiled by Tsinghua University, the accuracy of which has been validated by extant researches (e.g., Ding et al., 2015), and the global inventory of the Emissions Database for Global Atmospheric Research (EDGAR) v4.2 (EC-JRC/PBL, 2011) for the USA.

For the comparison to the derived top-down estimates, a 8-year (2005–2012) average from CPED and a 4-year (2005, 2007, 2009, and 2010) average from eGRID for the ozone season are used for power plants, of which the uncertainty is about 30 % (Liu et al., 2015) for CPED and 10 % for eGRID (5 % arises from continuous emissions monitoring systems (Gluck et al., 2003) and another 5 % arises from yearly variations in emissions after 2010), respectively. In addition, the mean emissions for the ozone season of the years 2005–2012 in MEIC and the mean annual emissions for the years 2005–2008 in EDGAR are used for cities, of which the uncertainty is estimated to be within a factor of 0.5 and 2 according to

the MEIC and EDGAR expert judgment of "medium magnitude of uncertainty" (Olivier et al., 2002). The bottom-up urban emissions derived from regional/global inventories have larger uncertainties compared to power plant emissions, primarily arising from the low-resolution activity rates/emission factors at regional level and the spatial allocation technique using surrogates to break regional-based emission data down to cities. Furthermore, temporal coverage of bottom-up emissions is limited, inducing additional uncertainties. For instance, a decline in NO$_2$ TVCDs from the years 2005–2008 to 2009–2013 with an average total reduction of 14 ± 9 % (mean $\pm$ standard variation) is detected for investigated US cities (Fig. S3). However, the most recent year available in EDGAR v4.2 is 2008, which cannot reflect the recent decline in NO$_x$ emissions, thus overestimating the average emissions.

For the comparison of bottom-up and top-down emissions for individual sites, the power plant inventories directly represent the stack emissions of individual facilities. For total city emissions, the gridded emission inventories have to be integrated over the metropolitan area for which the proposed top-down method is sensitive. Here, we define this area as 40×40 km^2, consistent with the considered interval v in Sect. 2.2.3. For the Pearl River Delta, we consider a larger interval of 120×120 km^2.

2.5 Selection of investigated sources

For this study, we choose large power plants and cities across China and the USA as the pre-selected candidates, of which bottom-up emission information is available from inventories described above. Power plants with NO$_x$ emission rates greater than 10 Gg yr^{-1} (CPED/eGRID) are investigated. Power plants located in urban areas (100 km around city cen-

ters) are excluded by visual inspection satellite imagery from Google Earth. The top 150 largest cities (rank in GDP/GDP per capita in 2013) in China and the 47 large US cities selected for analyses in Russell et al. (2012) were also examined. To assure a good fit performance, the following criteria have been defined: (1) the signal of the source is strong, i.e., the mean NO$_2$ TVCD in a circle of 100 km around the location center is larger than 1×10^{15} molec cm^{-2}; and (2) fit results with poor performance are discarded (see Sects. 2.2.2 and 2.2.3 for details). The number of wind direction sectors with a good lifetime fit performance is four on average. Table S2 of the Supplement provides a list of all sources under investigation which passed the criteria, including 24 power plants and 69 cities across China and the USA.

2.6 Impact of topography

The accuracy of fitted lifetimes is highly dependent on the accuracy of the a priori wind directions (used for "sorting" the satellite NO$_2$ observations) and velocities (used for converting x_0 into τ). However, accurate modeling of wind fields on small scales is challenging for large-scale models like ECMWF, which do not resolve urban scales. Consequently, wind fields might be biased in particular over complex mountainous terrain, related to the difficulties in resolving the characterization of small-scale orography in models (Beljaars et al., 2004).

We investigate the impact of topography by comparing ECMWF wind fields to 2005–2013 sounding measurements assembled by University of Wyoming (http://weather.uwyo.edu/upperair/sounding.html) and illustrate it for the cities of Harbin (plain terrain) and Taiyuan (mountainous city in Shanxi, China) in Fig. 4. In the top panels, topography used by ECMWF is compared to the topographic data from the 30 arc sec global land topography "GTOPO30" archived by the US Geological Survey (available at https://lta.cr.usgs.gov/GTOPO30, rescaled to 0.05°). Topographic variations are smeared out significantly by the topographic model used in ECMWF due to its coarser spatial resolution of 0.36°. The bottom panels show statistics for wind vectors below 500 m during daytime (12:00) and nighttime (00:00) from both ECMWF and the sounding measurements. The frequency distribution of wind directions (in 45° bins) shows a very good agreement in Harbin but not in Taiyuan: here southerly flows dominate according to sounding measurements, while easterly winds dominate in ECMWF.

We compared wind fields for cities where the fits work properly (Table S2) and the sounding measurements are available simultaneously, as presented in Table S3. For a mountainous city where the elevation in ECMWF contrasted sharply with that in GTOPO, Denver for instance, the correlation in wind speeds between ECMWF and sounding measurements is found to be much lower than for a non-mountainous city like Harbin.

Note that an error in a priori wind direction generally leads to a misclassification during the sorting of the satellite data (see also Sect. 3 of the Supplement). In such a case, the assumed wind component in direction of the sector is higher than the actual projection; if, for instance, the true wind would be 5 m s^{-1} from the north, but the model wind is 5 m s^{-1} from the east, the case is classified as easterly, while the actual easterly wind is 0. This leads to a systematic high biased projected wind speed in Eq. (4) and thus a low biased lifetime. Thus, mountainous sites often yield very low lifetimes (Table S2).
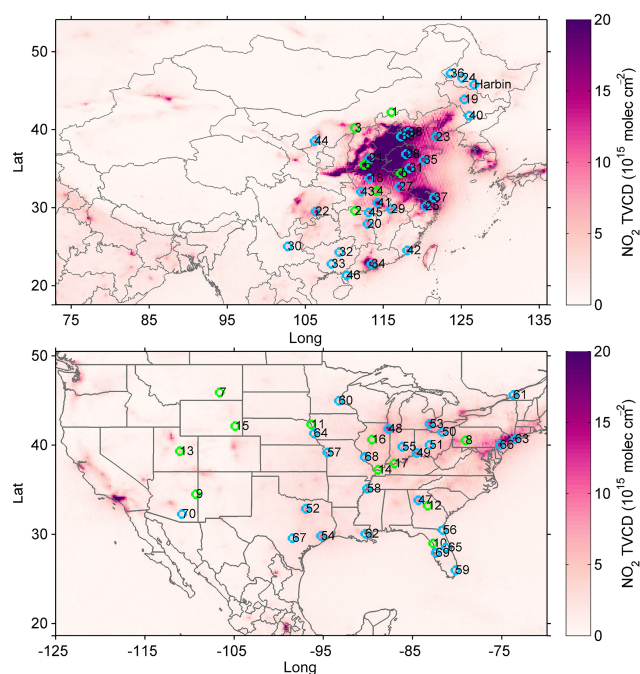
As the fitted lifetimes, and thus also emissions, rely on appropriate wind fields, we exclude mountainous sites from the following analysis. We simply define a site as mountainous where the absolute difference in elevation between ECMWF and GTOPO is larger than 250 m. A total of 7 power plants and 16 cities are rejected based on the criteria, as listed in Table S4. Seven sites in Table S3 fulfill this criteria and six of them present low correlation ($r^2 < 0.5$) in wind speeds between ECMWF and sounding measurements.

3 Results and discussion

We applied our modified method for determining NO$_x$ lifetimes and emissions to 17 power plants and 53 cities across China and the USA (see Fig. 5), which passed the criteria defined in Sects. 2.5 and 2.6. Some strong cities and power plants are not included as they are mountainous, e.g., Denver or Salt Lake City.
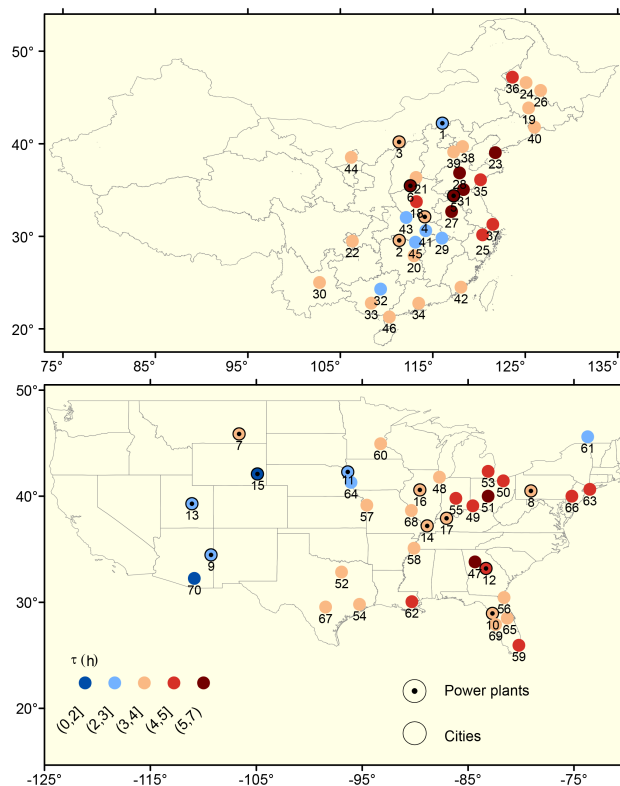
3.1 Lifetimes

Figure 6 illustrates the fitted NO$_x$ lifetimes for power plants and cities across China and the USA, which demonstrates the wide applicability of the modified method developed in this study. The derived lifetimes in "ozone season" (May–September) are 3.8 ± 1.0 h (mean $\pm$ standard deviation) on average with ranges of 1.8 to 7.5 h. These values are in agreement to previously reported NO$_x$ lifetimes (e.g., Beirle et al., 2004, 2011; Schaub et al., 2007; Valin et al., 2013) and correspond to a mean OH concentration of the order of 10^7 molecules cm^{-3} (Valin et al., 2013), which is a realistic number for a polluted urban plume around noon (e.g., Kramp and Volz-Thomas, 1997; Dillon et al., 2002; Hofzumahaus et al., 2009). For the investigated sites, the average lifetime for power plants (3.5 h) was found to be slightly shorter than for cities (3.9 h). Individual lifetimes have uncertainties of about 60 %. However, Fig. 6 still indicates that lifetimes are not completely random but rather show systematic spatial patterns. We could not unambiguously relate the variability of NO$_x$ lifetime to a driving parameter, like surface elevation, mean wind characteristics, or latitude. However, there is a tendency that NO$_x$ lifetime is longer in heavily polluted regions with higher NO$_2$ TVCDs, e.g., eastern China

Figure 5. Average OMI NO$_2$ TVCDs during ozone season (i.e., May to September) over China and the USA for the period 2005–2013. Green and blue symbols indicate the 17 power plants and 53 cities investigated in this work, respectively. Power plants and cities are labeled by their IDs (see Table S2).
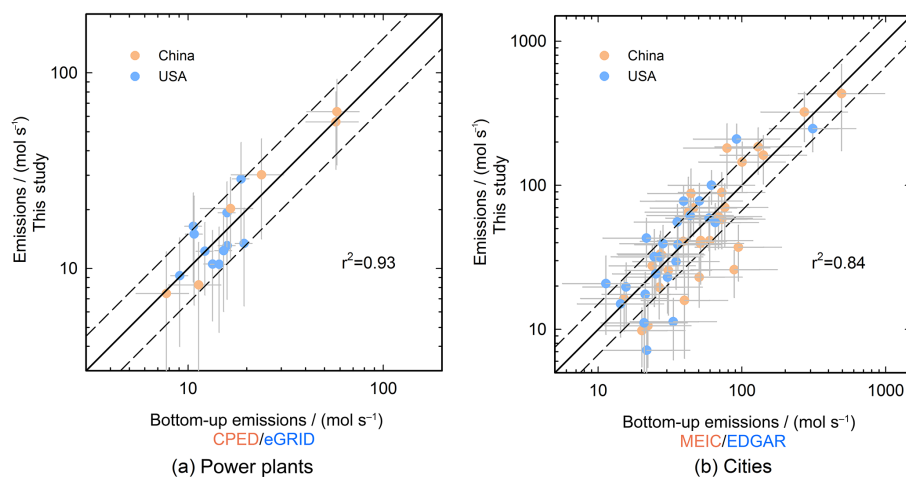

Figure 6. Fitted NO$_x$ lifetimes (color coded) for investigated emission sources over China and the USA. Locations of power plants are indicated by dots. Power plants and cities are labeled by their IDs (see Table S2).
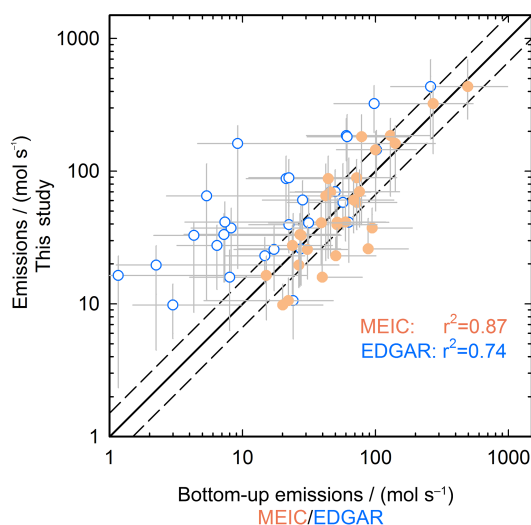
and eastern USA: the mean NO$_2$ TVCD for the ozone season in a circle with a radius of 100 km around sources with lifetimes over 5 h is 6.3×10^{15} molec cm^{-2}, while it is only 1.3×10^{15} molec cm^{-2} for sources with lifetime less than 2 h. This finding might be related to nonlinear NO$_x$ chemistry, resulting in a positive correlation between NO$_x$ lifetimes and NO$_2$ TVCDs when the concentration of NO$_x$ is high (Valin et al., 2013). However, we also find that a high NO$_x$ concentration does not necessarily correspond to a long lifetime, and the correlation between NO$_x$ lifetime and NO$_2$ TVCDs is rather low ($r^2 = 0.22$), probably due to the complex NO$_x$ chemistry, which is also affected by meteorological and chemical variability, like variations in UV flux, water vapor, and VOC levels. In addition, we used tropospheric HCHO columns from OMI (provided by BIRA; De Smedt et al., 2015) to investigate a potential link between VOCs and the estimated NO$_x$ lifetimes. We averaged the HCHO columns for the ozone season during 2005–2013 and explore their relationship with NO$_x$ lifetime. We observed systematic spatial patterns for the HCHO columns, e.g., the concentration of HCHO is higher in the eastern USA than the western USA, which is similar to the spatial distribution of NO$_x$ lifetime. However, the overall correlation between HCHO TVCDs and NO$_x$ lifetime is still rather low ($r^2 = 0.13$). Thus, we see no indication that VOCs are the main drivers for the spatial variability of NO$_x$ lifetime.

The proposed method estimates the mean lifetime basically from the change of NO$_2$ patterns for windy versus calm conditions. Valin et al. (2013) report on a dependency of the NO$_x$ lifetime on wind speed, with generally shorter lifetimes for higher wind speed. In addition, other factors, like the satellite's sensitivity (affected by, e.g., cloud properties or the vertical NO$_x$ profile) and the NO$_2$ background might change systematically between calm and windy conditions. In the fitted model function $N(x)$, a scaling factor a and an offset b are required in order to achieve a good fit performance for the individual fits, which probably compensate for these effects. However, on average, the derived values for a and b are close to 1 and 0, respectively: a is 0.9 ± 0.1 (mean $\pm$ standard deviation) and b is $0.0 \pm 0.1 \times 10^{23}$ molec cm^{-1} (mean $\pm$ standard deviation).

Thus, possible systematic effects due to all kind of changes between calm and windy conditions are small, and they are considered with a 10 % of contribution in the total uncertainty for NO$_x$ lifetimes (see Supplement).

We also performed an additional analysis of seasonal mean lifetimes (see Supplement, Fig. S4). Wintertime is excluded in the seasonal analysis, because in winter satellite data exhibit larger uncertainties and line densities under calm wind conditions are often unrepresentative of the emission pat-

Figure 7. Scatter plots of the derived NO$_x$ emissions for investigated **(a)** power plants and **(b)** cities versus bottom-up emission inventories. Emissions are given in mol s^{-1} calculated assuming a constant emission rate. Urban emissions from bottom-up inventories are integrated over 40 km × 40 km (see text). Error bars show the uncertainties for emissions by this method (see Sect. 2.3) and bottom-up inventories (see Sect. 2.4). The straight and dashed lines represent the ratio of 1 : 1 and 1.5 : 1/1 : 1.5, respectively.

Figure 8. Same as Fig. 7 but the derived NO$_x$ emissions for investigated cities versus MEIC and EDGAR estimates over China.

tern due to longer NO$_x$ lifetimes. The seasonal lifetimes reveal higher uncertainties due to a smaller number of available satellite observations compared to the ozone season and thus reduced number of wind direction sectors that yielding a valid fit. The uncertainty is sometimes too large to get reasonable seasonal patterns for a specific location. However, still a systematic seasonal variability can be observed for most non-mountainous cases: mean lifetimes are found to be shorter in summer (3.2 h) compared to spring (4.2 h) and autumn (4.5 h), as expected.
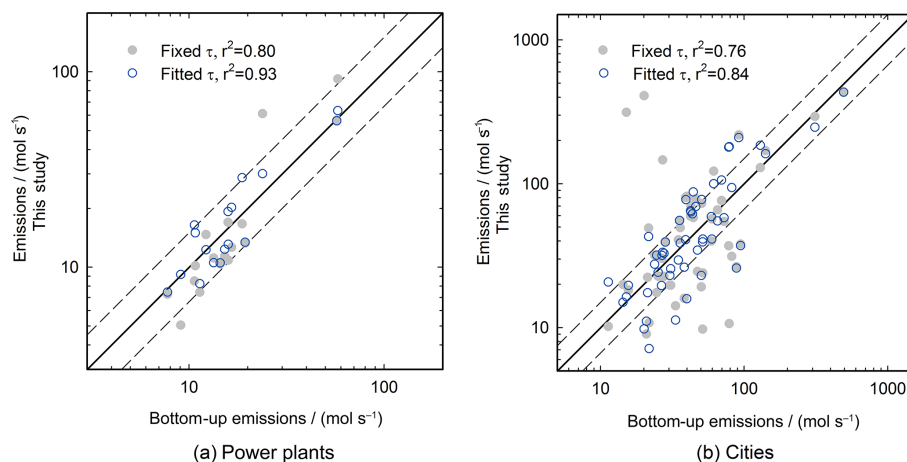
For some locations, the resulting emissions vary considerably over season, which again can be attributed to the poor

statistics; in particular spatial gaps can cause high uncertainties of the determined total NO$_2$ mass based on Eq. (5).

3.2 Emissions

Figure 7 compares the derived NO$_x$ emissions to bottom-up emission inventories (Sect. 2.4) for all 17 power plants and 53 cities. For power plants, the comparison (Fig. 7a) shows excellent agreement with a high correlation coefficient ($r^2 = 0.93$). Average emissions are 29 mol s^{-1} in bottom-up inventories and 31 mol s^{-1} in top-down estimates. The relative difference (defined as ($E_{\text{top down}} - E_{\text{bottom-up}})/E_{\text{bottom-up}}$) is within 30 % for most sites and 5 % ± 27 % (mean ± standard deviation) on average. For China and the USA, the relative differences are 4 % ± 18 % and 5 % ± 31 %, respectively, confirming the rather good agreement between CPED/eGRID bottom-up emission inventories and top-down estimates.

For the investigated cities, good agreement (Fig. 7b) between the derived emissions and the bottom-up emissions is reassuring and the r^2 reaches 0.84 (0.87 and 0.74 for China and the USA, respectively). The relative difference between derived NO$_x$ emissions and bottom-up emissions for cities is larger than that for power plants, reaching 9 % ± 49 % (1 % ± 46 % and 20 % ± 51 % for China and the USA, respectively) on average. This is probably related to the higher uncertainties of the bottom-up inventories for cities compared to those for power plants. Bottom-up emission inventories, developed by different researchers, often differ significantly from each other due to the application of various assumptions and extrapolations associated with their knowledge of activity data and emission factors. We further compared the representations of China's urban emissions between MEIC and EDGAR, as shown in Fig. 8. Huge discrep-

Figure 9. Scatter plots of the resulting NO$_x$ emissions for the investigated power plants and cities using fitted lifetimes (open circles) and fixed lifetimes (3.7 h) (filled circles) versus the respective estimates from bottom-up emission inventories. Emissions are given in molec/s calculated assuming a constant emission rate. The straight and dashed lines represent the ratio of 1 : 1 and 1.5 : 1/1 : 1.5, respectively.

ancies are found between EDGAR and top-down estimates (relative difference: 311 % ± 412 %) with large negative bias in the bottom-up inventories. Considering the deviation in national total NO$_x$ emissions is far less (20.7 and 24.9 Tg-NO$_2$ for 2008 in EDGAR and MEIC, respectively), the large bias could be primarily explained by the spatial distributions in the two inventories.

Both MEIC and EDGAR calculate emissions as province/country totals and distribute them to grids using spatial proxies. By comparing spatial proxies used in the two inventories, we identified the major differences in spatial allocation methods between them: (1) MEIC used an in-house high-resolution database (CPED) to represent power plant emissions in China while EDGAR used CARMA (Wheeler and Ummel, 2008). The coordinates of power plants in CARMA are highly uncertain for China (Liu et al., 2015); (2) for industrial emissions, MEIC first downscaled provincial totals to counties using industrial GDP and then allocated county emissions to grids with population density. EDGAR directly distributed provincial emissions by population density (EC-JRC/PBL, 2012) and (3) MEIC allocated on-road emissions by vehicle and road type using the China digital road-network map (Zheng et al., 2014), while EDGAR used the product of population density (Gridded Population of the World (GPW) version 3, CIESIN, 2005) and road network (the Global Roads Inventory Project (GRIP), PBL, 2008). All above factors are expected to contribute to the better representations of urban emissions in MEIC than in EDGAR over China and thus gain better agreement with top-down estimates.

It is interesting that EDGAR represents urban emissions much better in the USA than in China, even though EDGAR shared the same spatial allocation approach across different countries. One plausible explanation is that spatial proxies work better in the USA, implying the linear relation-

ships between emissions and proxies, e.g., vehicle emissions and road densities, industrial/residential emissions, and population densities. Different accuracy of spatial proxies among regions may also contribute to the discrepancy of performance in the two inventories. For instance, the GRIP database (http://geoservice.pbl.nl/website/GRIP/) missed too many roads for China (Fig. S6). By comparing with a high-resolution emission inventory, the Database of Road Transportation Emissions (DARTE), Gately et al. (2015) argued that EDGAR overestimated on-road emissions in city centers while underestimate at the suburban and exurban fringes, resulting from mismatches between road density and the actual spatial patterns of vehicle activity at urban scales. To better understand the uncertainties associated with the performance of spatial proxies, further source-by-source comparison is required between downscaled regional inventories and high-resolution inventories independent of spatial proxies (e.g., DARTE).

The emissions are derived based on the individual fitted lifetimes for each site. If, instead, the mean lifetime of all sites (3.7 h) would be considered for the calculation of emissions, the correlations to bottom-up emissions would be worse compared to the individual fitted NO$_x$ lifetime (Fig. 9). This holds for both power plants and cities. We conclude that variation of the fitted lifetime is not just the result of statistical noise, but it actually carries information on local variability of the oxidizing capacity of urban plumes. The individual lifetimes are thus well suited for the determination of emissions by a mass balance approach.

Satellite observations also enable the study of spatial and temporal distributions of SO$_2$ emissions (e.g., Fioletov et al., 2011) and even to obtain estimates of SO$_2$ lifetimes and emissions under special circumstances (e.g., Beirle et al., 2014; Fioletov et al., 2015). However, if the method developed in this study would be applied to SO$_2$ directly, higher

uncertainties have to be expected due to the longer lifetime of SO$_2$ (see Sect. 5 of the Supplement for a detailed discussion).

3.3 Uncertainties

Based on the approaches presented in Sect. 3 of the Supplement, we estimated that total uncertainties of NO$_x$ lifetime and emissions are within 39–80 % and 55–91 %, respectively, for all the investigated sites (see Sect. 2.5). For Harbin, relative uncertainties for mean lifetime and emissions are 43 and 58 %, respectively. However, it is worth noting that our uncertainty estimate is rather conservative. For power plants, relative differences between bottom-up and top-down estimates are all within 50 % (Fig. 7a). As bottom-up emission inventories for power plants are well developed with low uncertainties, the good consistency increases our confidence that the fitted emissions represent well the real-word emission characteristic. Thus, bottom-up inventories may have large biases for cities where emission estimates differ significantly from top-down constraints (i.e., the relative difference far exceeds 50 %).

From the quantitative analysis approach described in Sect. 2.3, we identify the uncertainties induced by individual factors. Detailed discussions are presented in the Supplement. In summary, we conclude that

- the uncertainty due to wind data is ∼ 30 % (affecting both τ and emissions)

- the effects of a possible systematic change of NO$_2$ TVCDs from calm (used for fit of E) to windy (used for fit of τ) conditions are small ($< 1,0$ %)

- the derived emissions (but not the lifetimes) are affected by the uncertainty of the NO$_2$ TVCDs (~ 30 %) and the NO$_x$ / NO$_2$ scaling factor (~ 10 %)

- the dependency on the definition of integration and fit intervals is about 10 %

- the CI of fitted lifetimes and total NO$_2$ mass is about 30 and 20 %, respectively; the standard mean error of fitted lifetimes for different wind directions is less than 40 % (see Sect. 3 of Supplement).

All involved uncertainties contain both statistical fluctuations as well as systematic effects. By ongoing satellite measurements (e.g., TROPOMI), i.e., longer available time periods, and the much better temporal sampling of upcoming geostationary satellite missions such as GEMS (Kim et al., 2012), TEMPO (Chance et al., 2012), or Sentinel-4 (Ingmann et al., 2012), statistical uncertainties will decrease. In addition, we expect further improvement of the presented lifetime fit method by using regional meteorological models that are more capable of representing wind fields in the planetary boundary layer especially for mountainous region. Also the uncertainties of TVCDs from satellite retrievals, which

is still the largest single component of total uncertainty in top-down emission estimates, is expected to decrease in the coming years: input data such as surface albedo or a priori profiles will improve, and the current intensive validation efforts (e.g., DISCOVER-AQ (http://discover-aq.larc.nasa.gov/) and AROMAT (http://uv-vis.aeronomie.be/aromat/)) will help to identify and remove systematic errors. It can thus be expected that total uncertainties of the proposed method will decrease significantly within the next decade.

4 Conclusions

We developed a new method to estimate NO$_x$ lifetimes and emissions of power plants and cities in polluted background from satellite NO$_2$ observations. The method improves upon that of Beirle et al. (2011) by explicitly accounting for interferences with neighboring strong NO$_x$ sources by using NO$_2$ spatial patterns under calm wind conditions as proxy of the patterns of emission sources. Lifetimes are derived from the change of NO$_2$ distributions under windy compared to calm conditions. NO$_x$ emissions are derived by mass balance: the total mass of NO$_2$ originating from the source of interest is divided by the lifetime derived for the corresponding source.

The new method for determining NO$_x$ lifetimes and emissions was applicable for 24 power plants and 69 cities over China and the USA, including 23 mountainous sites. We exclude the derived results for 23 mountainous sites from the analysis, which are expected to have larger uncertainties owing to the inaccurate wind data. The derived lifetimes for 70 non-mountainous sites are 3.8 ± 1.0 h (mean $\pm$ standard deviation) on average with ranges of 1.8 to 7.5 h. We observed systematic spatial patterns for the derived lifetimes; however they could not be simply explained by a specific driving parameter. Generally, higher lifetimes were found in heavily polluted regions, but the overall correlation between NO$_2$ TVCDs and NO$_x$ lifetime is quite low ($r^2 = 0.22$).

The derived top-down NO$_x$ emissions are generally in very good agreement with bottom-up emission inventories, in particular for power plants, while correlations for cities were lower, probably due to the higher uncertainty of the bottom-up inventories for cities. Compared to MEIC, the EDGAR global inventory significantly underestimated NO$_x$ emissions for Chinese cities, because spatial proxies used in EDGAR may misrepresent emission spatial patterns for China.

Owing to the global continuous monitoring of satellite measurements, this method can be applied to quantify the emissions from various cities and power plants even in polluted background around the world. For this study, we choose large sources across China and the USA as the pre-selected candidates, of which good-quality bottom-up emission information, particularly for power plants, is available. Further investigation on sources located in other regions, in particular Europe, will be performed in the near future, with collating the corresponding bottom-up emission inventories. This ca-

pability will further be enhanced with future satellite instrument like TROPOMI (Veefkind et al., 2012) featuring higher spatial resolution. In addition, upcoming geostationary satellite instruments will enable studies on the diurnal cycle of the NO$_x$ lifetime. More accurate estimates for emission rates, trends, and seasonality can be expected, which will serve as an independent data source to validate bottom-up emission estimates in the future.

Data availability

All data sets used here are publicly available and can be accessed through the links and references we have provided.

The Supplement related to this article is available online at doi:10.5194/acp-16-5283-2016-supplement.

References

Beirle, S., Platt, U., Wenig, M., and Wagner, T.: Weekly cycle of NO$_2$ by GOME measurements: a signature of anthropogenic sources, Atmos. Chem. Phys., 3, 2225–2232, doi:10.5194/acp-3-2225-2003, 2003.

Beirle, S., Platt, U., von Glasow, R., Wenig, M., and Wagner, T.: Estimate of nitrogen oxide emissions from shipping by satellite remote sensing, Geophys. Res. Lett., 31, L18102, doi:10.1029/2004GL020312, 2004.

Beirle, S., Boersma, K. F., Platt, U., Lawrence, M. G., and Wagner, T.: Megacity emissions and lifetimes of nitrogen oxides probed from space, Science, 333, 1737–1739, 2011.

Beirle, S., Hörmann, C., Penning de Vries, M., Dörner, S., Kern, C., and Wagner, T.: Estimating the volcanic emission rate and atmospheric lifetime of SO$_2$ from space: a case study for Kilauea volcano, Hawai'i, Atmos. Chem. Phys., 14, 8309–8322, doi:10.5194/acp-14-8309-2014, 2014.

Beljaars, A. C. M., Brown, A. R., and Wood, N.: A new parametrization of turbulent orographic form drag, Q. J. Roy. Meteorol. Soc., 130, 1327–1347, 2004.

Boersma, K. F., Eskes, H. J., Dirksen, R. J., van der A, R. J., Veefkind, J. P., Stammes, P., Huijnen, V., Kleipool, Q. L., Sneep, M., Claas, J., Leitão, J., Richter, A., Zhou, Y., and Brunner, D.: An improved tropospheric NO$_2$ column retrieval algorithm for the Ozone Monitoring Instrument, Atmos. Meas. Tech., 4, 1905–1928, doi:10.5194/amt-4-1905-2011, 2011.

Butler, T. M., Lawrence, M. G., Gurjar, B. R., van Aardenne, J., Schultz, M., and Lelieveld, J.: The representation of emissions from megacities in global emission inventories, Atmos. Environ., 42, 703–719, 2008.

Celarier, E. A., Brinksma, E. J., Gleason, J. F., Veefkind, J. P., Cede, A., Herman, J. R., Ionov, D., Goutail, F., Pommereau, J. P., Lambert, J. C., van Roozendael, M., Pinardi, G., Wittrock, F., Schönhardt, A., Richter, A., Ibrahim, O. W., Wagner, T., Bojkov, B., Mount, G., Spinei, E., Chen, C. M., Pongetti, T. J., Sander, S. P., Bucsela, E. J., Wenig, M. O., Swart, D. P. J., Volten, H., Kroon, M., and Levelt, P. F.: Validation of Ozone Monitoring Instrument nitrogen dioxide columns, J. Geophys. Res., 113, D15S15, doi:10.1029/2007JD008908, 2008.

Center for International Earth Science Information Network (CIESIN), Food and Agriculture Organization of the United Nations (FAO), and Centro Internacional de Agricultura Tropical (CIAT): Gridded Population of the World, version 3 (GPWv3): Population Count Grid, available at: http://sedac.ciesin.columbia.edu/data/set/gpw-v3-population-count (last accessed: 10 June, 2015), 2005.

Chance, K., Lui, X., Suleiman, R. M., Flittner, D. E., and Janz, S. J.: Tropspheric Emissions: Monitoring of Pollution (TEMPO), presented at the 2012 AGU Fall Meeting, San Francisco, USA, 3–7 December 2012, A31B-0020, 2012.

de Foy, B., Wilkins, J. L., Lu, Z., Streets, D. G., and Duncan, B. N.: Model evaluation of methods for estimating surface emissions and chemical lifetimes from satellite data, Atmos. Environ., 98, 66–77, 2014.

de Foy, B., Lu, Z., Streets, D. G., Lamsal, L. N., and Duncan, B. N.: Estimates of power plant NO$_x$ emissions and lifetimes from OMI NO$_2$ satellite retrievals, Atmos. Environ., 116, 1–11, 2015.

Dee, D. P., Uppala, S. M., Simmons, A. J., Berrisford, P., Poli, P., Kobayashi, S., Andrae, U., Balmaseda, M. A., Balsamo, G., Bauer, P., Bechtold, P., Beljaars, A. C. M., van de Berg, L., Bidlot, J., Bormann, N., Delsol, C., Dragani, R., Fuentes, M., Geer, A. J., Haimberger, L., Healy, S. B., Hersbach, H., Hólm, E. V., Isaksen, L., Kållberg, P., Köhler, M., Matricardi, M., McNally, A. P., Monge-Sanz, B. M., Morcrette, J. J., Park, B. K., Peubey, C., de Rosnay, P., Tavolato, C., Thépaut, J. N., and Vitart, F.: The ERA-Interim reanalysis: configuration and performance of the data assimilation system, Q. J. Roy. Meteorol. Soc., 137, 553–597, 2011.

De Smedt, I., Stavrakou, T., Hendrick, F., Danckaert, T., Vlemmix, T., Pinardi, G., Theys, N., Lerot, C., Gielen, C., Vigouroux, C., Hermans, C., Fayt, C., Veefkind, P., Müller, J.-F., and Van

Roozendael, M.: Diurnal, seasonal and long-term variations of global formaldehyde columns inferred from combined OMI and GOME-2 observations, Atmos. Chem. Phys., 15, 12519–12545, doi:10.5194/acp-15-12519-2015, 2015.

Dillon, M. B., Lamanna, M. S., Schade, G. W., Goldstein, A. H., and Cohen, R. C.: Chemical evolution of the Sacramento urban plume: Transport and oxidation, J. Geophys. Res., 107, ACH 3-1–ACH 3-15, doi:10.1029/2001JD000969, 2002.

Ding, J., van der A, R. J., Mijling, B., Levelt, P. F., and Hao, N.: NO$_x$ emission estimates during the 2014 Youth Olympic Games in Nanjing, Atmos. Chem. Phys., 15, 9399–9412, doi:10.5194/acp-15-9399-2015, 2015.

Duncan, B. N., Yoshida, Y., de Foy, B., Lamsal, L. N., Streets, D. G., Lu, Z., Pickering, K. E., and Krotkov, N. A.: The observed response of Ozone Monitoring Instrument (OMI) NO$_2$ columns to NO$_x$ emission controls on power plants in the United States: 2005–2011, Atmos. Environ., 81, 102–111, 2013.

European Commission (EC): Joint Research Centre (JRC)/Netherlands Environmental Assessment Agency (PBL), Emission Database for Global Atmospheric Research (EDGAR), release version 4.2, available at: http://edgar.jrc.ec.europa.eu (last access: 1 December 2013), 2011.

European Commission (EC): Joint Research Centre (JRC)/Netherlands Environmental Assessment Agency (PBL), Global emission inventories in the Emission Database for Global Atmospheric Research (EDGAR) – Manual (I) Gridding: EDGAR emissions distribution on global gridmaps, available at: http://publications.jrc.ec.europa.eu/repository/bitstream/JRC78261/edgarv4_manual_i_gridding_pubsy_final.pdf (last accessed: 1 June, 2015), 2012.

Fioletov, V. E., McLinden, C. A., Krotkov, N., Moran, M. D., and Yang, K.: Estimation of SO$_2$ emissions using OMI retrievals, Geophys. Res. Lett., 38, L21811, doi:10.1029/2011gl049402, 2011.

Fioletov, V. E., McLinden, C. A., Krotkov, N., and Li, C.: Lifetimes and emissions of SO$_2$ from point sources estimated from OMI, Geophys. Res. Lett., 42, 2015GL063148, doi:10.1002/2015gl063148, 2015.

Gately, C. K., Hutyra, L. R., and Sue Wing, I.: Cities, traffic, and CO$_2$: A multidecadal assessment of trends, drivers, and scaling relationships, P. Natl. Acad. Sci., 112, 4999–5004, 2015.

Gluck, S., Glenn, C., Logan, T., Vu, B., Walsh, M., and Williams, P.: Evaluation of NO$_x$ flue gas analyzers for accuracy and their applicability for low-concentration measurements, J. Air Waste Manage. Assoc., 53, 749–758, 2003.

Hilboll, A., Richter, A., and Burrows, J. P.: Long-term changes of tropospheric NO$_2$ over megacities derived from multiple satellite instruments, Atmos. Chem. Phys., 13, 4145–4169, doi:10.5194/acp-13-4145-2013, 2013.

Hofzumahaus, A., Rohrer, F., Lu, K., Bohn, B., Brauers, T., Chang, C.-C., Fuchs, H., Holland, F., Kita, K., Kondo, Y., Li, X., Lou, S., Shao, M., Zeng, L., Wahner, A., and Zhang, Y.: Amplified Trace Gas Removal in the Troposphere, Science, 324, 1702–1704, 2009.

Ingmann, P., Veihelmann, B., Langen, J., Lamarre, D., Stark, H., and Courrèges-Lacoste, G. B.: Requirements for the GMES Atmosphere Service and ESA's implementation concept: Sentinels-4/-5 and -5p, Remote Sens. Environ., 120, 58–69, 2012.

Jacob, D. J., Heikes, E. G., Fan, S. M., Logan, J. A., Mauzerall, D. L., Bradshaw, J. D., Singh, H. B., Gregory, G. L., Talbot, R. W., Blake, D. R., and Sachse, G. W.: Origin of ozone and NO$_x$ in the tropical troposphere: A photochemical analysis of aircraft observations over the South Atlantic basin, J. Geophys. Res., 101, 24235–24250, doi:10.1029/96jd00336, 1996.

Kim, J.: GEMS (Geostationary Enviroment Monitoring Spectrometer) onboard the GeoKOMPSAT to monitor air quality in high temporal and spatial resolution over Asia-Pacific region, presented at the 2012 EGU General Assembly, Vienna, Austria, 22–27 April 2012, EGU2012-4051, 2012.

Kim, S. W., Heckel, A., Frost, G. J., Richter, A., Gleason, J., Burrows, J. P., McKeen, S., Hsie, E. Y., Granier, C., and Trainer, M.: NO$_2$ columns in the western United States observed from space and simulated by a regional chemistry model and their implications for NO$_x$ emissions, J. Geophys. Res., 114, D11301, doi:10.1029/2008jd011343, 2009.

Konovalov, I. B., Beekmann, M., Richter, A., and Burrows, J. P.: Inverse modelling of the spatial distribution of NO$_x$ emissions on a continental scale using satellite data, Atmos. Chem. Phys., 6, 1747–1770, doi:10.5194/acp-6-1747-2006, 2006.

Kramp, F. and Volz-Thomas, A.: On the Budget of OH Radicals and Ozone in an Urban Plume from the Decay of C5–C8 Hydrocarbons and NO$_x$, J. Atmos. Chem., 28, 263–282, 1997.

Lamsal, L. N., Martin, R. V., Padmanabhan, A., van Donkelaar, A., Zhang, Q., Sioris, C. E., Chance, K., Kurosu, T. P., and Newchurch, M. J.: Application of satellite observations for timely updates to global anthropogenic NO$_x$ emission inventories, Geophys. Res. Lett., 38, L05810, doi:10.1029/2010gl046476, 2011.

Lelieveld, J., Beirle, S., Hörmann, C., Stenchikov, G., and Wagner, T.: Abrupt recent trend changes in atmospheric nitrogen dioxide over the Middle East, Sci. Adv., 1, e1500498, doi:10.1126/sciadv.1500498, 2015.

Leue, C., Wenig, M., Wagner, T., Klimm, O., Platt, U., and Jähne, B.: Quantitative analysis of NO$_x$ emissions from Global Ozone Monitoring Experiment satellite image sequences, J. Geophys. Res., 106, 5493–5505, doi:10.1029/2000JD900572, 2001.

Levelt, P. F., van den Oord, G. H. J., Dobber, M. R., Malkki, A., Huib, V., Johan de, V., Stammes, P., Lundell, J. O. V., and Saari, H.: The ozone monitoring instrument, Geoscience and Remote Sensing, IEEE Transactions on, 44, 1093–1101, 2006.

Lin, J.-T., Liu, Z., Zhang, Q., Liu, H., Mao, J., and Zhuang, G.: Modeling uncertainties for tropospheric nitrogen dioxide columns affecting satellite-based inverse modeling of nitrogen oxides emissions, Atmos. Chem. Phys., 12, 12255–12275, doi:10.5194/acp-12-12255-2012, 2012.

Liu, F., Zhang, Q., Tong, D., Zheng, B., Li, M., Huo, H., and He, K. B.: High-resolution inventory of technologies, activities, and emissions of coal-fired power plants in China from 1990 to 2010, Atmos. Chem. Phys., 15, 13299–13317, doi:10.5194/acp-15-13299-2015, 2015.

Lu, Z., Streets, D. G., de Foy, B., Lamsal, L. N., Duncan, B. N., and Xing, J.: Emissions of nitrogen oxides from US urban areas: estimation from Ozone Monitoring Instrument retrievals for 2005–2014, Atmos. Chem. Phys., 15, 10367–10383, doi:10.5194/acp-15-10367-2015, 2015.

Martin, R. V., Jacob, D. J., Chance, K., Kurosu, T. P., Palmer, P. I., and Evans, M. J.: Global inventory of nitrogen oxide emis-

sions constrained by space-based observations of NO$_2$ columns, J. Geophys. Res., 108, 4537, doi:10.1029/2003jd003453, 2003.

Martin, R. V., Sioris, C. E., Chance, K., Ryerson, T. B., Bertram, T. H., Wooldridge, P. J., Cohen, R. C., Neuman, J. A., Swanson, A., and Flocke, F. M.: Evaluation of space-based constraints on global nitrogen oxide emissions with regional aircraft measurements over and downwind of eastern North America, J. Geophys. Res., 111, D15308, doi:10.1029/2005JD006680, 2006.

Netherlands Environmental Assessment Agency (PBL), Global Roads Inventory Project (GRIP) database, avalable at: http://geoservice.pbl.nl/website/GRIP/ (last access: 15 June, 2015), 2008.

Olivier, J., Peters, J., Bakker, J., Berdowski, J., Visschedijk, A., and Bloos, J.: Applications of EDGAR. Including a description of EDGAR 3.2. Reference database with trend data for 1970–1995, Rijksinstituut voor Volksgezondheid en Milieu RIVM, Bilthoven (the Netherlands), 2002.

Platt, U.: Differential optical absorption spectroscopy (DOAS) in: Air monitoring by spectroscopic techniques, edited by: Sigrist, M. W., John Wiley and Sons, New York, 27–76, 1994.

Richter, A., Burrows, J. P., Nusz, H., Granier, C., and Niemeier, U.: Increase in tropospheric nitrogen dioxide over China observed from space, Nature, 437, 129–132, 2005.

Russell, A. R., Valin, L. C., Bucsela, E. J., Wenig, M. O., and Cohen, R. C.: Space-based constraints on spatial and temporal patterns of NO$_x$ emissions in California, 2005–2008, Environ. Sci. Technol., 44, 3608–3615, 2010.

Russell, A. R., Valin, L. C., and Cohen, R. C.: Trends in OMI NO$_2$ observations over the United States: effects of emission control technology and the economic recession, Atmos. Chem. Phys., 12, 12197–12209, doi:10.5194/acp-12-12197-2012, 2012.

Schaub, D., Brunner, D., Boersma, K. F., Keller, J., Folini, D., Buchmann, B., Berresheim, H., and Staehelin, J.: SCIAMACHY tropospheric NO$_2$ over Switzerland: estimates of NO$_x$ lifetimes and impact of the complex Alpine topography on the retrieval, Atmos. Chem. Phys., 7, 5971–5987, doi:10.5194/acp-7-5971-2007, 2007.

Schneider, P. and van der A, R. J.: A global single-sensor analysis of 2002–2011 tropospheric nitrogen dioxide trends observed from space, J. Geophys. Res., 117, D16309, doi:10.1029/2012jd017571, 2012.

Seinfeld, J. H. and Pandis, S. N.: Atmospheric chemistry and physics: From air pollution to climate change, John Wiley and Sons, New York, 204–275, 2006.

USEPA: Technical support document for the 9th edition of eGRID with year 2010 data (the Emissions & Generation Resource Integrated Database), Washington, D.C., 2014.

Valin, L. C., Russell, A. R., and Cohen, R. C.: Variations of OH radical in an urban plume inferred from NO$_2$ column measurements, Geophys. Res. Lett., 40, 1856–1860, doi:10.1002/grl.50267, 2013.

Valin, L. C., Russell, A. R., and Cohen, R. C.: Chemical feedback effects on the spatial patterns of the NO$_x$ weekend effect: a sensitivity analysis, Atmos. Chem. Phys., 14, 1–9, doi:10.5194/acp-14-1-2014, 2014.

Veefkind, J. P., Aben, I., McMullan, K., Förster, H., de Vries, J., Otter, G., Claas, J., Eskes, H. J., de Haan, J. F., Kleipool, Q., van Weele, M., Hasekamp, O., Hoogeveen, R., Landgraf, J., Snel, R., Tol, P., Ingmann, P., Voors, R., Kruizinga, B., Vink, R., Visser, H., and Levelt, P. F.: TROPOMI on the ESA Sentinel-5 Precursor: A GMES mission for global observations of the atmospheric composition for climate, air quality and ozone layer applications, Remote Sens. Environ., 120, 70–83, 2012.

Wheeler, D. and Ummel, K.: Calculating CARMA: Global estimation of CO$_2$ emissions from the power sector, Working Paper 145, Center for Global Development, Washington, DC, 2008.

Zhao, Y., Wang, S., Duan, L., Lei, Y., Cao, P., and Hao, J.: Primary air pollutant emissions of coal-fired power plants in China: Current status and future prediction, Atmos. Environ., 42, 8442–8452, 2008.

Zhao, Y., Nielsen, C. P., Lei, Y., McElroy, M. B., and Hao, J.: Quantifying the uncertainties of a bottom-up emission inventory of anthropogenic atmospheric pollutants in China, Atmos. Chem. Phys., 11, 2295–2308, doi:10.5194/acp-11-2295-2011, 2011.

Zheng, B., Huo, H., Zhang, Q., Yao, Z. L., Wang, X. T., Yang, X. F., Liu, H., and He, K. B.: High-resolution mapping of vehicle emissions in China in 2008, Atmos. Chem. Phys., 14, 9787–9805, doi:10.5194/acp-14-9787-2014, 2014.